JOURNAL OF AIRCRAFT
Vol. 29, No. 3, May–June 1992

Transonic Aeroelasticity Analysis for Rotor Blades

Lie-Mine Gea* and Chuen-Yen Chow†
University of Colorado, Boulder, Colorado 80309
and
I-Chung Chang‡
NASA Ames Research Center, Moffett Field, California 94035

A numerical method is presented for calculating the unsteady transonic rotor flow with aeroelasticity effects. The blade structural dynamic equations based on beam theory were formulated by the finite element method and were solved in the time domain instead of the frequency domain. A global-local coordinate-transformation matrix was used to reduce the inaccuracy caused by large blade deformations. A new structure code was developed and was validated by comparing the computed natural frequencies with experimental data of a model rotor blade. For different combinations of precone, droop, and pitch, the correlations are very good in the first three flapping modes and the first twisting mode. However, the predicted frequencies are too high for the first lagging mode at high rotational speeds. This new structure code has been coupled into a transonic rotor flow code, TFAR2, to demonstrate the capability of treating elastic blades in transonic rotor flow calculations. The flowfields for a model-scale rotor in both hover and forward flight are calculated. Results show that the blade elasticity significantly affects the flow characteristics in forward flight.

Nomenclature

A = blade cross-section area
a = local speed of sound
a_∞ = far-field speed of sound
a_0–a_5 = coefficients in Newmark method
$\tilde{a}_0,\tilde{a}_1$ = constants for Rayleigh damping
$[C]$ = element damping matrix
$[\boldsymbol{C}]$ = damping matrix for the blade
c = blade chord length
E = Young's modulus
G = shear modulus
$[G]$ = rotational matrix for entire blade
I_y,I_z = blade cross-section moments of inertia about y and z axes, respectively
J = torsional rigidity
$[K]$ = stiffness matrix for the blade
$[K]_E$ = nonrotating element stiffness matrix
$[K]_G$ = element geometric stiffness matrix
$[K]_{GT}$ = element geometric-stiffness-like matrix
l = blade element length
$[M]$ = element mass matrix
$[\boldsymbol{M}]$ = mass matrix for the blade
$\boldsymbol{n}$ = unit vector normal to the blade surface
$P(t)$ = aerodynamic load vector
$\boldsymbol{q}$ = flow velocity
q_i = generalized coordinates
$[R]$ = rotational matrix for an element
T = total kinetic energy of the sytem
t = time
U = total strain energy of the system
$\tilde{U}$ = strain energy due to twisting motion induced by centrifugal force
u_x,u_y,u_z = elastic displacements in x, y, and z axes, respectively
x,y,z = blade-fixed global coordinates
x',y',z' = blade-fixed local coordinates
x_i = local coordinate within an element
α,δ = Newmark parameters
γ = specific heat ratio (1.4 for air)
$\theta_x,\theta_y,\theta_z$ = elastic rotational angles with respect to x, y, and z axes
μ = advance ratio
ξ_n = nth mode damping ratio
ρ = blade density
ϕ = velocity potential
$[\phi]$ = jump in velocity potential
ω = blade rotational speed

Introduction

THE rotor flowfield contains very complicated unsteady, viscous, and three-dimensional flow phenomena. For each revolution, the blade may enter a transonic flow regime on the advancing side and may exhibit boundary-layer separation on the retreating side. Blade-vortex interaction will occur when the blade encounters the wakes shed from other blades. The blade elastic deformations make the flowfield even more complex.

Recently, there have been extensive developments in rotor flow computations. Most of them apply small disturbance approximations along the mean surface.[1,2] Some advanced computational works have used finite-difference or finite-volume schemes to simulate the rotor flow by solving the potential,[3–6] Euler,[7–9] or Navier-Stokes equations. In these computer codes the rotor blade is assumed to be rigid; therefore, the aeroelastic effect is neglected. For a rotor blade, as the aspect ratio is increased, the aerodynamic-dependent elastic effect becomes more important and needs to be included in the flow calculations for a better prediction.

Presented as Paper 89-2212 at the AIAA 7th Applied Aerodynamics Conference, Seattle, WA, July 31–Aug. 2, 1989; received Jan. 29, 1990; revision received Feb. 20, 1991; accepted for publication March 27, 1991.

*Research Associate, Department of Aerospace Engineering Sciences, Campus Box 429. Member AIAA.
†Professor, Department of Aerospace Engineering Sciences, Campus Box 429. Associate Fellow AIAA.
‡Research Scientist. MS 258-1 Member AIAA.

A number of analyses have been conducted to study the rotor blade aeroelasticity. Houbolt and Brooks[10] derived the partial differential equations for blade motions by linear analysis. Hodges and Dowell[11] then developed the equations to second order, where the ordering scheme was adopted to neglect higher order terms. In recent years, the finite-element method has become a more popular tool to solve rotor dynamics problems. Different approaches have been successfully applied for different purposes. For example, Friedmann and Straub[12] used a local Galerkin-type finite element and modal analysis to study the stability of a rotary wing. Sivaneri and Chopra[13] applied Hamilton's principle to the equations of blade motion, given in Ref. 11, for the finite-element formulation to simulate the bearingless rotor blade.

The main purpose of this work is to develop a finite element code that can be efficiently coupled with a flow solver to implement the aeroelasticity effect for rotor flow calculations. Hamilton's principle is applied to derive the finite-element equations. The energy expressions are derived from beam theory consideration and may not be as inclusive as Hodges and Dowell's derivations, but the term-by-term manipulations are physically more meaningful.

For the transonic problem in the presence of shock waves, the flow equations are nonlinear. The traditional assumption of constant mass and stiffness matrices for subsonic problems may not be accurate enough for large amplitudes of motion. To describe the blade-surface boundary condition more precisely, a global-local coordinate-transformation matrix is derived to improve the computational accuracy.

The computed system natural frequencies for a model rotor blade in the first three flapping modes, the first lagging mode, and the first twisting mode will be compared with experimental results[14] to validate the structure code.

In the present work, a full-potential code, TFAR2, with only planar wake, is modified to couple with the structure code. A potential code without a good wake modeling cannot make good predictions for a lifting case, which is necessary for elastic calculations. However, a qualitative rather than a quantitative analysis is attempted in this work, so the computation time efficiency for a potential code becomes the biggest advantage of the current study.

So far, very few coupling works[15,16] have been published. In these works, a loose iteration procedure was used to couple the aerodynamic and structural codes. However, TFAR2 is able to treat exact blade geometry, and it includes not only the twist but also the flapping, lagging, and axial extension information to make the coupling procedure more realistic. Some preliminary results for both hover and forward flight are presented to show the elastic effect in transonic rotor calculations.

Aerodynamic Model

In the current computational model, a single blade on the advancing side with transonic effects is considered and the flow is assumed to be inviscid, irrotational, and isentropic. A velocity potential ϕ exists, and the complete equation for this velocity potential is

$$\phi_{tt} + [(\nabla\phi)^2]_t + \nabla\phi \cdot \nabla\left[\frac{1}{2}(\nabla\phi)^2\right] = a^2\nabla^2\phi \tag{1}$$

Bernoulli's equation, relating a and ϕ, is

$$\phi_t + \frac{1}{2}(\nabla\phi)^2 + \frac{a^2}{\gamma - 1} = \frac{a_\infty^2}{\gamma - 1} \tag{2}$$

Then the equation is solved in a blade-fixed frame, also called the moving frame. The relative velocity between inertial and moving frame is

$$\boldsymbol{V} = \boldsymbol{U} + \boldsymbol{\Omega} \times \boldsymbol{r} \tag{3}$$

where $\boldsymbol{U}$ and $\boldsymbol{\Omega}$ are the linear and angular velocities of the moving frame relative to the inertial frame, and $\boldsymbol{r}$ is the position vector. The potential equation in the moving frame can then be written as

$$\phi_{tt} + 2\boldsymbol{V}\cdot\nabla\phi_t + (\boldsymbol{V}\cdot\nabla)(\boldsymbol{V}\cdot\nabla\phi) + \nabla\phi\cdot\boldsymbol{V}_t + 2\nabla\phi\cdot\nabla\phi_t + (\boldsymbol{V}\cdot\nabla)[(\nabla\phi)^2] + \nabla\phi\cdot\nabla\left[\frac{1}{2}(\nabla\phi)^2\right] = a^2\nabla^2\phi \tag{4}$$

Bernoulli's equation becomes

$$\phi_t + \boldsymbol{V}\cdot\nabla\phi + \frac{1}{2}(\nabla\phi)^2 + \frac{a^2}{\gamma - 1} = \frac{a_\infty^2}{\gamma - 1} \tag{5}$$

Several boundary conditions are needed to complete the boundary value problem. The boundary condition on the rotor blade surface is

$$\boldsymbol{q}\cdot\boldsymbol{n} = 0$$

where $\boldsymbol{q}$ is the velocity in the moving frame. A simple planar wake model is used, in which the wake is represented by a vortex sheet shed from the trailing edge. On the sheet

$$[\phi_t] + \boldsymbol{q}_m\cdot\nabla[\phi] = 0 \tag{6}$$

where $\boldsymbol{q}_m$ is the mean of upper and lower velocities at each point on the vortex sheet. At the far flowfield the boundary condition is formulated as Neumann condition so that the time derivatives of the velocity potential vanish along the characteristic of the flow in each spanwise plane:

$$\phi_t + \boldsymbol{q}_a\cdot\nabla\phi = 0 \tag{7}$$

where $\boldsymbol{q}_a$ is the outgoing eigenvelocity of the flow equation in each spanwise plane.

The equation is then solved in a parabolic sheared-mesh system, and an ADI scheme is performed for the unsteady solutions. The details can be found in Ref. 6.

Structure Dynamic Model

For the current model, an engineering type of approach is used, and the beam theory is applied. The matrices for a nonrotating blade are first derived; then the extra terms due to the rotational effect are implemented.

Consider a beam type of rotor-blade element with two nodes, each node having six degrees of freedom. Figure 1 shows the element geometry and the corresponding nodal forces. From Hamilton's principle, in generalized coordinates q_i, which are the degrees of freedom of the element in this case, the well-known Lagrange equations can be derived:

$$\frac{\mathrm{d}}{\mathrm{d}t}\left(\frac{\partial T}{\partial \dot{q}_i}\right) - \frac{\partial T}{\partial q_i} + \frac{\partial U}{\partial q_i} = Q_i, \quad (i = 1, \ldots, n) \tag{8}$$

where Q_i represents the generalized forces.

Shape Functions

Before we start to derive the matrices, it is necessary to introduce the shape functions N_i for our element, which define the displacements within an element while the ith degree of freedom of the element has unit value and all others are zero. Let

$$\xi = x_i/l$$

where l is the length of the element and x_i is the local coordinate within an element, measured from one end of the element.

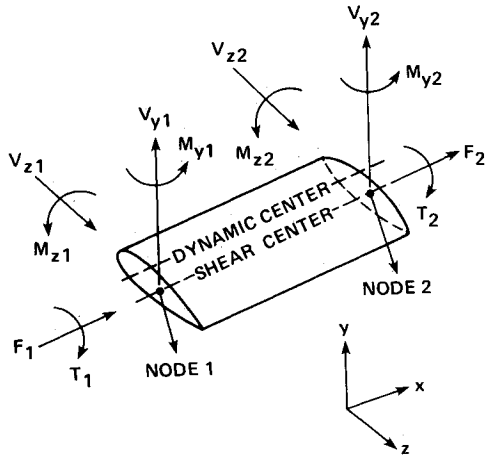

Fig. 1 Blade element geometry and nodal forces.

Flapping:

$$\begin{aligned} N_{F1} &= 1 - 3\xi^2 + 2\xi^3 \\ N_{F2} &= l\xi - 2l\xi^2 + \xi^3 \\ N_{F3} &= 3\xi^2 - 2l\xi^3 \\ N_{F4} &= -l\xi^2 + l\xi^3 \end{aligned} \tag{9}$$

Lagging:

$$\begin{aligned} N_{L1} &= 1 - 3\xi^2 + 2\xi^3 \\ N_{L2} &= -l\xi + 2l\xi^2 - \xi^3 \\ N_{L3} &= 3\xi^2 - 2l\xi^3 \\ N_{L4} &= l\xi^2 - l\xi^3 \end{aligned} \tag{10}$$

Axial extension:

$$\begin{aligned} N_{A1} &= 1 - \xi \\ N_{A2} &= \xi \end{aligned} \tag{11}$$

Twisting:

$$\begin{aligned} N_{T1} &= 1 - \xi \\ N_{T2} &= \xi \end{aligned} \tag{12}$$

where subscripts F, L, T, and A denote the flapping, lagging, twisting, and axial directions, and 1 and 2 represent two element nodes.

Mass Matrix

The kinetic energy for a blade element can then be written as

$$T = \frac{1}{2}\int_0^l \int_0^C [(\dot{u}_y + z\dot{\theta}_x)^2 + \dot{u}_z^2 + \dot{u}_x^2]\, dm \tag{13}$$

where the displacements, expressed in terms of shape functions, are

$$u_y = (N_{F1}, N_{F2}, N_{F3}, N_{F4}) \begin{pmatrix} u_{y1} \\ \theta_{z1} \\ u_{y2} \\ \theta_{z2} \end{pmatrix}$$

$$u_z = (N_{C1}, N_{C2}, N_{C3}, N_{C4}) \begin{pmatrix} u_{z1} \\ \theta_{y1} \\ u_{z2} \\ \theta_{y2} \end{pmatrix}$$

$$\theta_x = (N_{T1}, N_{T2}) \begin{pmatrix} \theta_{x1} \\ \theta_{x2} \end{pmatrix}$$

$$u_x = (N_{A1}, N_{A2}) \begin{pmatrix} u_{x1} \\ u_{x2} \end{pmatrix}$$

By applying Lagrange's equations we can generate the 12 × 12 mass matrix $[M]$ for each element, which corresponds to the inertial forces of the system. In the current model, the coupling effect between flapping and twisting is included by allowing the blade cross-section elastic center to be different from the mass center.

Stiffness Matrix

The strain energy for a nonrotating rotor blade element can be written as

$$U = \frac{1}{2}\int_0^l (EAu_{x,x}^2 + EI_z u_{y,xx}^2 - EI_y u_{z,xx}^2 + GJ\theta_{x,x}^2)\, dx \tag{14}$$

Again, Lagrange's equations yield a 12 × 12 stiffness matrix $[K]_E$ that corresponds to the strain forces of the system.

For a rotor system, the large centrifugal force due to rotation will increase strain energy and cause additional stiffness. This stiffness, called geometry stiffness, is independent of structural elastic properties and depends only on the element's geometry and external loading. It is denoted by $[K]_G$ and can be determined by considering a beam element that is subjected to a centrifugal force in the axial direction. It is then applied to both flapping and lagging directions. The detailed derivations can be found in Ref. 17.

In addition, the centrifugal force has some implicit contributions in the twisting degree of freedom. If a blade rotates with a constant rotational speed ω, every point on the cross section is subjected to a centrifugal force in a slightly different direction, as shown in Fig. 2. For an untwisted blade, the difference of centrifugal forces acting through an arbitrary point A and the elastic center EC is

$$\bar{f} = \rho\, dA\, dx\, a\omega^2$$

where dA is an area segment, and a is the distance between A and EC. Since $\bar{f}$ lies on the cross-section plane and points from A to EC, it can be decomposed into y and z components

$$\bar{f}_y = \rho\, dA\, dx\, (-y)\omega^2$$

$$\bar{f}_z = \rho\, dA\, dx\, (-z)\omega^2$$

The resultant torque is found to be zero after integration over the cross section. However, the additional forces

$$\Delta\bar{f}_y = \bar{f}_y\theta$$

$$\Delta\bar{f}_z = \bar{f}_z\theta$$

are induced if the cross section rotates by a small angle θ (see Fig. 2). The corresponding strain energy becomes

$$d\bar{U} = d\bar{T}\,(\theta)/2 = \frac{1}{2}\rho\, dA\, dx\, \theta^2\omega^2(y^2 + z^2)$$

where $d\bar{T}$ is the resulting torque due to $\Delta\bar{f}_y$ and $\Delta\bar{f}_z$. Integrating $d\bar{U}$ over the element and introducing the linear shape functions for the twisting degree of freedom, we obtain

$$\bar{U} = \frac{\omega^2}{4}\rho J\left(\frac{2}{3}\theta_1^2 + \frac{2}{3}\theta_1\theta_2 + \frac{2}{3}\theta_2^2\right)$$

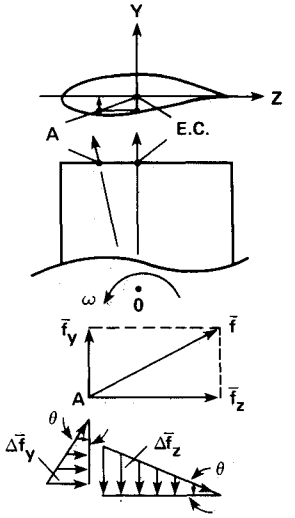

Fig. 2 Centrifugal force direction and additional forces due to blade twist.

where J is the cross-section moment of inertia with respect to the elastic center. Then by applying Lagrange's equation, the geometric-stiffness-like matrix corresponding to the twisting degree of freedom can be obtained:

$$[K]_{GT} = \frac{\omega^2 l}{6}\rho J\begin{bmatrix}2 & 1\\ 1 & 2\end{bmatrix} \tag{15}$$

Combining $[K]_E$, $[K]_G$, and $[K]_{GT}$, we can write the final stiffness matrix for an element symbolically as

$$[K] = [K]_E + [K]_G + [K]_{GT} \tag{16}$$

Damping Matrix

Usually, the damping matrix can be represented as[18]

$$C = M\sum_b \bar{a}_b[M^{-1}K]^b$$

Here, the Rayleigh damping, with $b = 1$ in the previous equation, is adopted:

$$[C] = \bar{a}_0[M] + \bar{a}_1[K] \tag{17}$$

The values of $\bar{a}_0$ and $\bar{a}_1$ can be determined by

$$\xi_n = \frac{1}{2\omega_n}\sum_b \bar{a}_b\omega_n^{2b}$$

where ξ_n is the nth mode damping ratio, which is usually obtained from experiment. Only two equations are needed to solve for $\bar{a}_0$ and $\bar{a}_1$.

Now we have the mass, stiffness, and damping matrices for an element. The dynamic equations for the entire blade can then be assembled by considering displacement compatibility conditions at element boundary. This yields

$$[M]\ddot{q}(t) + [C]\dot{q}(t) + [K]q(t) = P(t) \tag{18}$$

where $P(t)$ is the aerodynamic load vector. For each element, it consists of 12 nodal forces (see Fig. 1).

Geometric Nonlinearity

In transonic flow or in high-advance-ratio forward flight, large deformations can be expected, and the integrated solutions based on constant structure coefficients may not be accurate enough because of the geometric nonlinearity. To improve the accuracy, a global/local coordinate transformation is usually used.

Let (x,y,z) and $x',y',z')$ represent global and local coordinate systems, respectively, for a blade element. For the ith degree of freedom of the element we can write

$$q_{il} = [R]q_{ig} \tag{19}$$

where subscripts g and l indicate the global and local coordinate system, and $[R]$ is the rotational matrix

$$[R] = \begin{bmatrix}\cos\theta_{x'x} & \cos\theta_{x'y} & \cos\theta_{x'z}\\ \cos\theta_{y'x} & \cos\theta_{y'y} & \cos\theta_{y'z}\\ \cos\theta_{z'x} & \cos\theta_{z'y} & \cos\theta_{z'z}\end{bmatrix} \tag{20}$$

In the previous matrix, $\theta_{x'x}$ is the rotation angle from axis x to axis x', and so on. The rotational matrix for the entire element becomes

$$[G] = \begin{bmatrix}[R] & & & \\ & [R] & & \\ & & [R] & \\ & & & [R]\end{bmatrix} \tag{21}$$

The element mass and stiffness matrices, formulated in the local system, can be transferred to the global system by using the energy expression

$$\begin{aligned}[M]_g &= [G]^T[M]_l[G]\\ [K]_g &= [G]^T[K]_l[G]\end{aligned} \tag{22}$$

The dynamic equation is then solved in the global system.

Dynamic Equation Solver

A numerical integration scheme is used to solve the dynamic equations. In the current work, the Newmark method, an extension of the linear-acceleration method, is adopted. To deal with large defomations, we apply the Newmark method in incremental form as follows:

$$[M]\Delta\ddot{q} + [C]\Delta\dot{q} + [K]\Delta q = \Delta P \tag{23}$$

$$\begin{aligned}\ddot{q}(t+\Delta t) &= \ddot{q}(t) + \Delta\ddot{q}(t)\\ \dot{q}(t+\Delta t) &= \dot{q}(t) + \Delta\dot{q}(t)\\ &= \dot{q}(t)\\ &\quad + [(1-\delta)\ddot{q}(t) + \delta\ddot{q}(t+\Delta t)]\Delta t\\ q(t+\Delta t) &= q(t) + \Delta q(t)\\ &= q(t) + \dot{q}(t)\Delta t\\ &\quad + \left[\left(\frac{1}{2}-\alpha\right)\ddot{q}(t) + \alpha\ddot{q}(t+\Delta t)\right]\Delta t^2\end{aligned}$$

where α and δ are Newmark parameters that are used to control the accuracy and stability. Here $\delta = 0.5$ and $\alpha = 0.25$, which were originally proposed by Newmark as uncon-

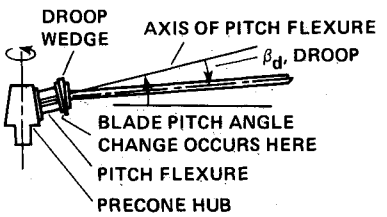

Fig. 3 Experimental model rotor configuration.

Table 1 Comparison between computed and experimental natural frequencies

	RPM	1st Flap	2nd Flap	3rd Flap	1st Edge	1st Tor.
Precone = 0.0, Droop = 0.0, Pitch = 0.0						
EXP	0	5.21	32.17	91.80	24.02	43.61
FEM	0	5.18	32.48	91.22	23.38	44.82
EXP	400	9.53	36.69	95.89	24.30	45.00
FEM	400	9.28	37.28	96.19	24.64	45.32
EXP	600	12.75	42.37	101.95	24.50	44.31
FEM	600	12.58	42.53	102.03	26.12	45.93
EXP	800	16.30	49.40	109.30	24.71	48.50
FEM	800	16.03	48.92	109.66	28.06	46.76
EXP	1000	19.52	55.93	117.41	25.09	47.93
FEM	1000	19.54	56.07	117.95	30.06	47.82
Precone = 5.0, Droop = 0.0, Pitch = 0.0						
EXP	0	5.19	32.28	90.58	23.78	44.14
FEM	0	5.19	32.48	91.23	23.38	43.16
EXP	1000	20.32	55.12	116.72	24.50	48.64
FEM	1000	19.53	56.07	118.70	30.36	46.27
Precone = 0.0, Droop = 5.0, Pitch = 0.0						
EXP	0	5.21	32.36	91.31	23.91	44.24
FEM	0	5.19	32.48	91.23	23.38	43.16
EXP	1000	19.37	55.30	114.34	24.48	53.74
FEM	1000	19.53	56.07	118.70	30.36	46.27
Precone = 5.0, Droop = 0.0, Pitch = 12.0						
EXP	0	5.17	32.22	90.62	23.63	43.95
FEM	0	5.19	32.49	91.23	23.38	43.16
EXP	1000	18.71	54.62	117.04	24.79	50.27
FEM	1000	19.52	56.06	118.69	30.36	46.26

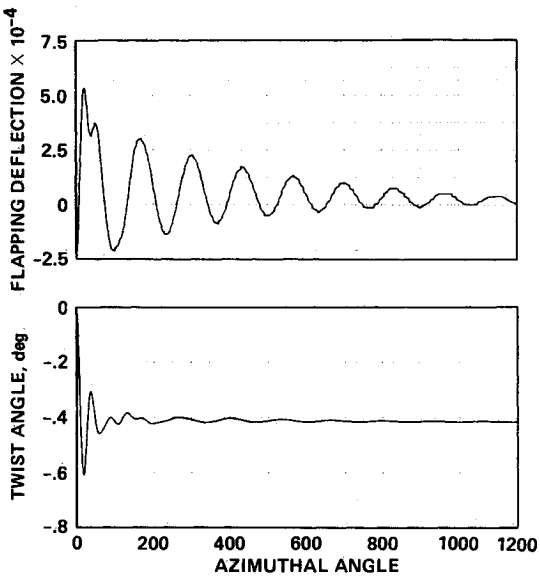

Fig. 4 Blade tip deflection plot for hovering case; α_0 = 5 deg, M_T = 0.75.

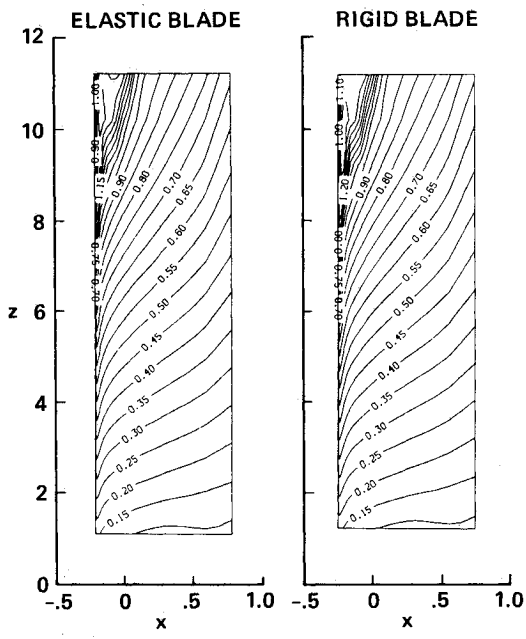

Fig. 5 Comparison of upper surface Mach contours for hovering rigid and elastic blades; α_0 = 5 deg, M_T = 0.75.

ditionally stable. Substituting $\Delta\ddot{q}(t)$, $\Delta\dot{q}(t)$ and $\Delta q(t)$ into Eq. (23) gives

$$\Delta q(t)\,([K] + a_0[M] + a_1[C]) = \Delta P + [M][a_2\dot{q}(t) + a_3\ddot{q}(t)] + [C][a_4\dot{q}(t) + a_5\ddot{q}(t)]$$

where

$$a_0 = \frac{1}{\alpha\Delta t^2}, \quad a_1 = \frac{\delta}{\alpha\Delta t}, \quad a_2 = \frac{1}{\alpha\Delta t}$$

$$a_3 = \frac{1}{2\alpha}, \quad a_4 = \frac{\delta}{\alpha}, \quad a_5 = \left(\frac{\delta}{2\alpha}\right)\Delta t$$

From the previous equations, the displacement increments $\Delta q(t)$ are solved, where $\dot{q}(t)$ and $\ddot{q}(t)$ are the velocities and accelerations at the current time step. Then the increments of velocity and acceleration are

$$\Delta\dot{q}(t) = a_1\Delta q(t) - a_4\dot{q}(t) - a_5\ddot{q}(t)$$

$$\Delta\ddot{q}(t) = a_0\Delta q(t) - a_2\dot{q}(t) - a_3\ddot{q}(t)$$

The displacements, velocities, and accelerations for the next time step can then be obtained, and this process is repeated.

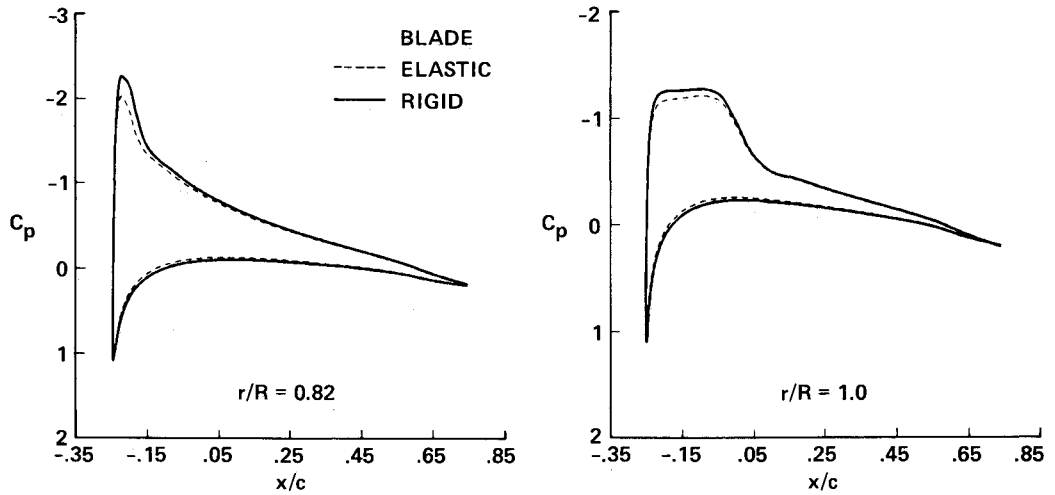

Fig. 6 Comparison of C_p plots at two sections, r/R = 0.82 and 1.0, for hovering rigid and elastic blades; α_0 = 5 deg, M_T = 0.75.

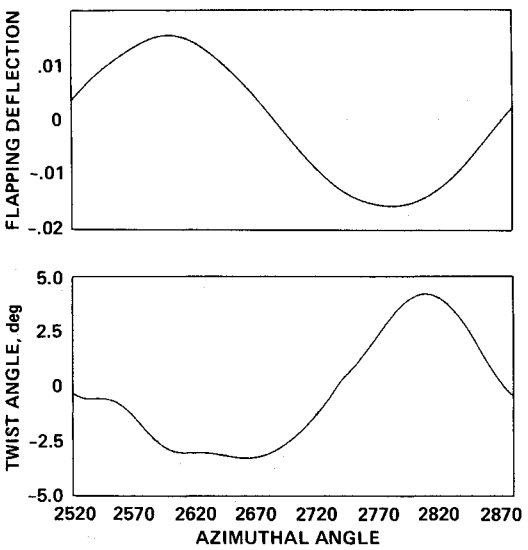

Fig. 7 Blade tip deflection plot for forward flight case; α_0 = 5 deg, M_T = 0.6, μ = 0.25.

Structure Code Validation

To validate the structure code, an isolated and hingeless two-bladed model helicopter rotor blade (see Fig. 3) is simulated by the current code. The torsionally soft rotor blade has a NACA 0012 airfoil with neither twist not taper. The rotor configuration, the blade properties, and the experimental setup details can be found in Ref. 14. Four cases with stiff pitch flexure at different rotational speeds are considered: 1) precone = 0 deg, droop = 0 deg, pitch = 0 deg; 2) precone = 5 deg, droop = 0 deg, pitch = 0 deg; 3) precone = 0 deg, droop = 5 deg, pitch = 0 deg; and 4) precone = 0 deg, droop = 5 deg, pitch = 12 deg. The computed natural frequencies for the first three flapping modes, the first torsion mode, and the first lagging mode are compared with experimental data in Table 1. The correlation is very good for most of the modes. For the first three flapping modes, the frequencies are within 4% of the experimental values. For the torsion mode, the frequencies are excellent for case 1 and fair for the other cases. The most unsatisfactory frequencies are in the lagging modes, where the code predicts higher frequencies for high rpm cases. The error is mainly from the inaccurate modeling for centrifugal force in the lagging motion. The blade lagging motion is within the rotational plane; in this it is essentially different from the flapping motion, but in the present analysis, identical modifications were used in both the flapping and the lagging directions. However, the

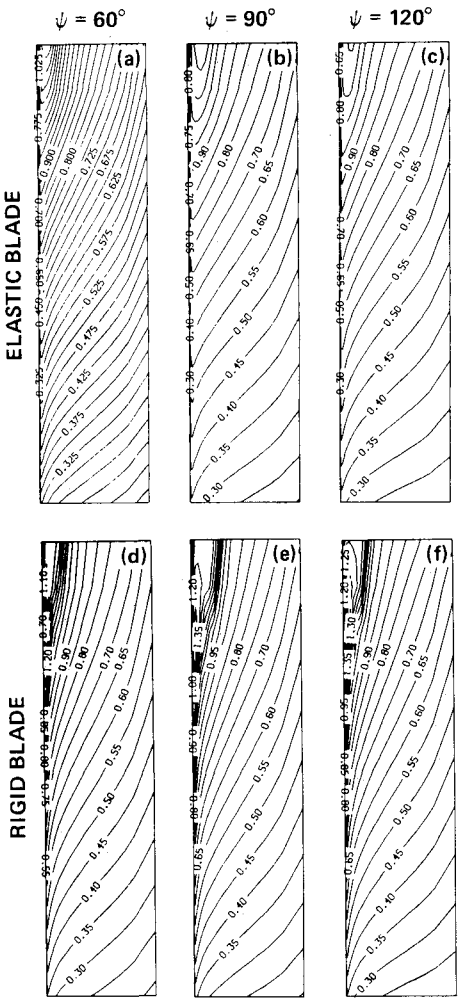

Fig. 8 Comparison of upper surface Mach contours at three different azimuth angles, ψ = 60, 90, and 120 deg, for rigid and elastic blades in forward flight; α_0 = 5 deg, M_T = 0.6, μ = 0.25.

experimental data in case 1 show that the variation in lagging mode is very limited, only 4.4% from 0 to 1000 rpm, so the predicted lagging motion may still be acceptable even without the centrifugal force modification.

Code Coupling

The following procedure is performed to couple the TFAR2 code and the structure code to complete the aeroelastic analysis.

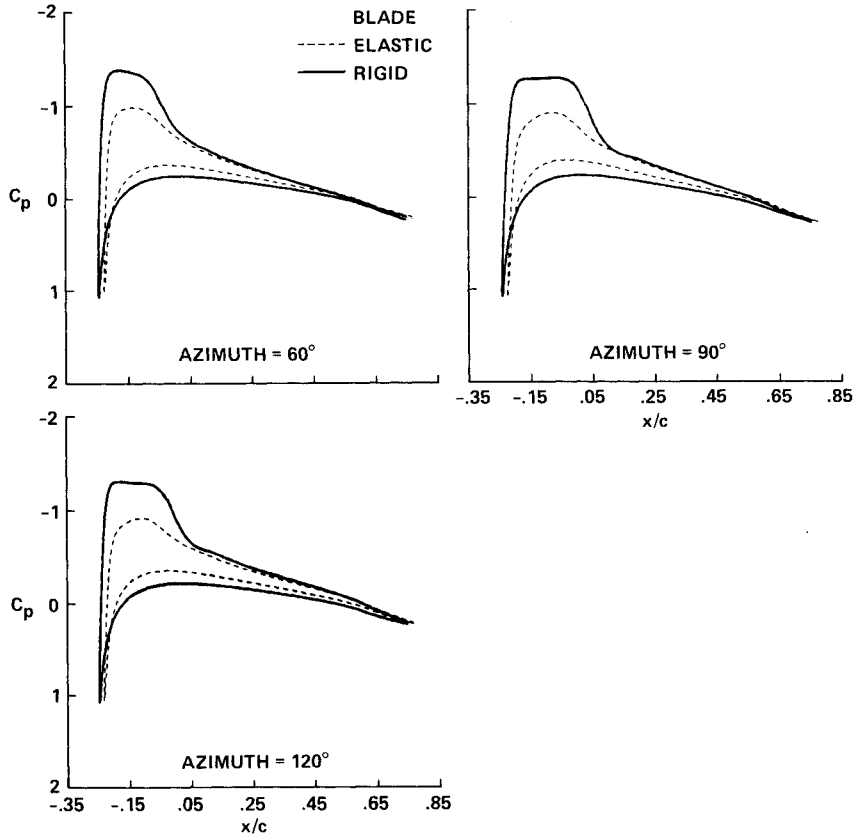

Fig. 9 Comparison of tip C_p plots at three different azimuthal angles, ψ = 60, 90, and 120 deg, for rigid and elastic blades in forward flight; α_0 = 5 deg, M_T = 0.6, μ = 0.25.

1) The full-potential transonic rotor flow equations are solved by the TFAR2 code, and the blade sectional lift, drag, and moment are calculated.

2) The aerodynamic forces are converted to the corresponding element nodal forces by applying element shape functions and using Gauss integration.

3) The structural dynamic equation is rotated from the local to the global coordinate system and integrated by Newmark's method to obtain the element nodal displacements.

4) The deformed blade geometry is read into TFAR2, and a new grid system with new surface boundary conditions is generated for the next step in the aerodynamic calculations. Steps 1 through 4 are repeated until the desired conditions are reached.

Numerical Results

Calculations were carried out for an experimental scale model of a rotor that is the same as the one used in frequency comparisons. The aspect ratio for this blade is about 11, and the blade is divided into 8 elements for the finite element model. In the aerodynamic computations, a C-H type finite-difference grid (96 × 16 × 32 in chordwise, vertical, and spanwise directions) was used. To complete one revolution for the aforementioned grid and element, 30 min of CPU time on the Cray X-MP computer is required. The computation time for elastic calculation is, in general, less than 3% of that for the aerodynamic calculation.

Two sets of numerical results, for both 1) hover and 2) forward flight, are presented to show the blade dynamic response due to the aerodynamic forces and the flow calculations with and without elastic effect.

Hover Case

The first set of results is for a hovering case in which the initial pitch is 5 deg and the blade-tip Mach number M_T is 0.75. Figure 4 shows the time history, represented by the azimuth angle, of the flapping and twisting motions of the blade tip. It shows that for the current coupling it takes about three revolutions for the solutions to converge. The blade elastic deformations approach constant values after the blade reaches its balanced position, and hence the flow becomes steady state. The unsteady part of the solution at the beginning stage of the calculation is caused mainly by the "coupling." After the solution is converged, there is about −0.4 deg of twist and a bend-up at the blade tip. Figure 5 compares the blade-upper-surface Mach contours in rigid and elastic calculations. A slightly smaller transonic regime was found on the elastic blade surface. In Fig. 6, the pressure distributions for rigid and elastic blades at two span stations, r/R = 0.82 and = 1.0, are compared; the difference is small and the shock structure remains almost the same.

Forward Flight Case

The second set of results is for forward flight with 5 deg blade initial pitch. The flow condition is M_T = 0.6 and the advance ratio μ = 0.25. Figure 7 shows the converged solution of the blade-tip deformations. The blade oscillates with a mean position, and the twist angle varies from about −3.0 deg on the advancing side to 4.0 deg on the retreating side. This elastic phenomenon will dramatically affect the results of flow predictions. Figure 8 shows the advancing-side, upper-surface Mach contours for rigid and elastic blades at three different azimuth angles. We can see that for the elastic blade, the Mach number at the tip is much lower than that at the rigid blade. The pressure distributions around the tip section for rigid and elastic blades at three different azimuth angles are compared in Fig. 9. A significant difference in C_p distributions was found; the elastic case also predicts a much weaker shock.

Conclusions

A new finite element rotor dynamic code has been developed, and the code has been validated by comparing the computed natural frequencies favorably with experimental

data. In general, the correlation is very good for most of the modes in four different cases, as can be seen from Table 1. The lagging mode at high rotational speed is not as good; however, this discrepancy might be overcome by using a better centrifugal-force model in lagging motion.

The structure code has been coupled with the transonic-rotor-flow code (TFAR2) to study the aeroelastic effect in transonic regime for both hover and forward flight. According to the numerical results, the elastic effect for the hover case is not as important as it is for forward flight. For forward flight, even at a low advance ratio, the blade elastic response due to unsteady aerodynamic forces is significant, and the elastic blade consideration is needed for accurate flow predictions.

Acknowledgments

This work was sponsored by NASA Ames Research Center under cooperative Agreement No. NCC 2-508. The first author wishes to thank T. J. Tzong of McDonnell Douglas at Long Beach for his valuable discussions.

References

[1]Caradonna, F. X., and Isom, M. P., "Numerical Calculation of Unsteady Transonic Potential Flow over Helicopter Rotor Blades," *AIAA Journal*, Vol. 14, No. 4, 1976, pp. 428–488.

[2]Chattot, J. J., "Calculation of Three-Dimensional Unsteady Transonic Flows past Helicopter Blades," NASA TP-1721, Oct. 1980.

[3]Arieli, R., and Tauber, M. E., "Computation of Subsonic and Transonic Flow about Lifting Rotor Blades," AIAA Paper 79-1667, 1979.

[4]Strawn, R. C., and Caradonna, F. X., "Numerical Modeling of Rotor Flows with a Conservative Form of the Full-Potential Equations," AIAA Paper 86-0079, 1986.

[5]Sankar, R. C., and Prichard, D., "Solution of Transonic Flow past Rotor Blades Using Conservative Full-Potential Equation," AIAA Paper 85-5012, 1985.

[6]Chang, I.-C., "Transonic Flow Analysis for Rotors, Part 2—Three-Dimensional, Unsteady, Full-Potential Calculation." NASA TP-2375, 1985.

[7]Roberts, T. W., and Murman, E. M., "Solution Method for a Hovering Helicopter Rotor Using the Euler Equations," AIAA Paper 85-0436, 1985.

[8]Chang, I.-C., and Tung, C., "Euler Solution of the Transonic Flow for a Helicopter Rotor," AIAA Paper 87-0523, Jan. 1987.

[9]Chen, C. L., McCroskey, W. J., and Ying, S. X., "Euler Solution of Multiblade Rotor Flow," Thirteenth European Rotorcraft Forum, Arles, France, Sept. 1987.

[10]Houbolt, J. C., and Brooks, G. W., "Differential Equations of Motion for Combined Flapwise Bending, Chordwise Bending, and Torsion of Twisted Nonuniform Rotor Blades," NACA Rept. 1346, 1958.

[11]Hodges, D. H., and Dowell, E. H., "Nonlinear Equations of Motion for the Elastic Bending and Torsion of Twisted Nonuniform Rotor Blades," NASA TN D-7818, Dec. 1974.

[12]Friedmann, P. P., and Straub, F., "Application of the Finite Element Method for Rotary-Wing Aeroelasticity," *Journal of the American Helicopter Society*, Vol. 25, No. 1, 1980, pp. 36–44.

[13]Sivaneri, N. T., and Chopra, I., "Finite Element Analysis for Bearingless Rotor Blade Aeroelasticity," *Journal of the American Helicopter Society*, Vol. 29, No. 2, 1984, pp. 42–51.

[14]Srinivasan, A. V., Cutts, D. G., and Shu, H. T., "An Experimental Investigation of the Structure Dynamics of a Torsionally Soft Rotor in Vacuum," NASA CR-177418, July 1986.

[15]Yamauchi, G. K., Heffernan, R. M., and Gaubert, M., "Correlation of SA349/2 Helicopter Flight Test Data with a Comprehensive Rotorcraft Model," Paper 74 Twelfth European Rotorcraft Forum, Garmisch-Partenkirchen, Germany, Sept. 1986.

[16]Kim, K. C., Desopper, A., and Chopra, I., "Blade Response Calculations Using Three-Dimensional Aerodynamic Modeling," Journal of the American Helicopter Society, Vol. 36, No. 1, 1991, pp. 68–77.

[17]Cook, R., *Concepts and Applications of Finite Element Analysis*, Wiley, New York, 1981.

[18]Clough, R. W., and Penzien, J., *Dynamics of Structures*, McGraw-Hill, New York, 1975.